RESEARCH ARTICLE

ADVANCED MATERIALS TECHNOLOGIES
www.advmattechnol.de

Self-Boosting Energy Generation via Triboelectric Nanogenerator–Capacitor Coupling

Jihye Kim, Hanjun Ryu, SeongMin Kim, Hyeon Yeong Lee, Armine Karami, Dimitri Galayko, Donghyeon Kang, Sung Soo Kwak, Hong-Joon Yoon, Philippe Basset, and Sang-Woo Kim**

With the development of wearable and wireless electronic devices, the triboelectric nanogenerator (TENG) is attracting interest as a candidate for portable power. Many studies are conducted to increase the surface charge density of the TENG, such as external charge pumping or external electron excitation strategies. However, there are limitations in that another additional external energy source is required. Here, a TENG–capacitor (TC) coupling system that can maximize energy generation and storage efficiency within a limited volume is proposed. Density functional theory calculations indicate that the electric field induced on capacitor increases the fermi energy of positive triboelectric material, resulting in more charge transfer between two triboelectric materials. TC coupling system enhances TENG output performance and the capacitor charging rate in a virtuous cycle. This study provides new insights into TENG structural design and an important guideline for the use of TENG as a portable power source for wearable and wireless applications.

1. Introduction

Recently, with the development of wearable electronic devices and wireless sensor networks, off-grid electricity is required.[1–3] Because big data and the Internet of Things are rapidly being developed, nanogenerators and sustainable energy harvesting technologies are being actively studied.[4–5] Among the energy harvesters, the triboelectric nanogenerator (TENG) based on triboelectrification and electrostatic induction effects that convert mechanical energy into electrical energy has attracted worldwide interest.[6–11] The TENG is widely used for micro/nano power, self-powered sensors, high voltage applications, and blue energy harvesting owing to its advantages of low cost, lightweight, various material selections, simple preparation, and high voltage and current peak density.[12–20] Because the surface charge density on triboelectric layers determines the performance of the TENG, many studies have been conducted to increase its value. In previous studies, the surface charge density was improved using various methods, such as material selection,[21–23] surface treatment,[24–25] and ion implantation.[26] However, there were limitations in that the surface charge density inevitably decreased owing to leakage current of dielectric material and air breakdown.[22,25,26] High-vacuum and high-pressure gas

---

J. Kim
Center for Bio-Integrated Electronics
Northwestern University
Evanston, IL 60208, USA

H. Ryu
Department of Advanced Materials Engineering
Chung-Ang University
Anseong 17546, Republic of Korea

H. Ryu
Department of Intelligence Energy and Industry
Chung-Ang University
Seoul 06974, Republic of Korea

S. Kim, S.-W. Kim
Department of Materials Science and Engineering
Center for Human-oriented Triboelectric Energy Harvesting
Yonsei University
Seoul 03722, Republic of Korea
E-mail: kimsw1@yonsei.ac.kr

The ORCID identification number(s) for the author(s) of this article can be found under https://doi.org/10.1002/admt.202301309

DOI: 10.1002/admt.202301309

H. Y. Lee, D. Kang
School of Advanced Materials Science and Engineering
Sungkyunkwan University
Suwon 16419, Republic of Korea

A. Karami, P. Basset
ESYCOM
University of Gustave Eiffel
CNRS
Marne-la-Vallée F-77454, France
E-mail: philippe.basset@esiee.fr

D. Galayko
LIP6 Laboratory
Sorbonne University
Paris 75004, France

S. S. Kwak
Bionics Research Center of Biomedical Research Division
Korea Institute of Science and Technology
Seoul 02792, Republic of Korea

H.-J. Yoon
Department of Electronic Engineering
Gachon University
Seongnam 13120, Republic of Korea

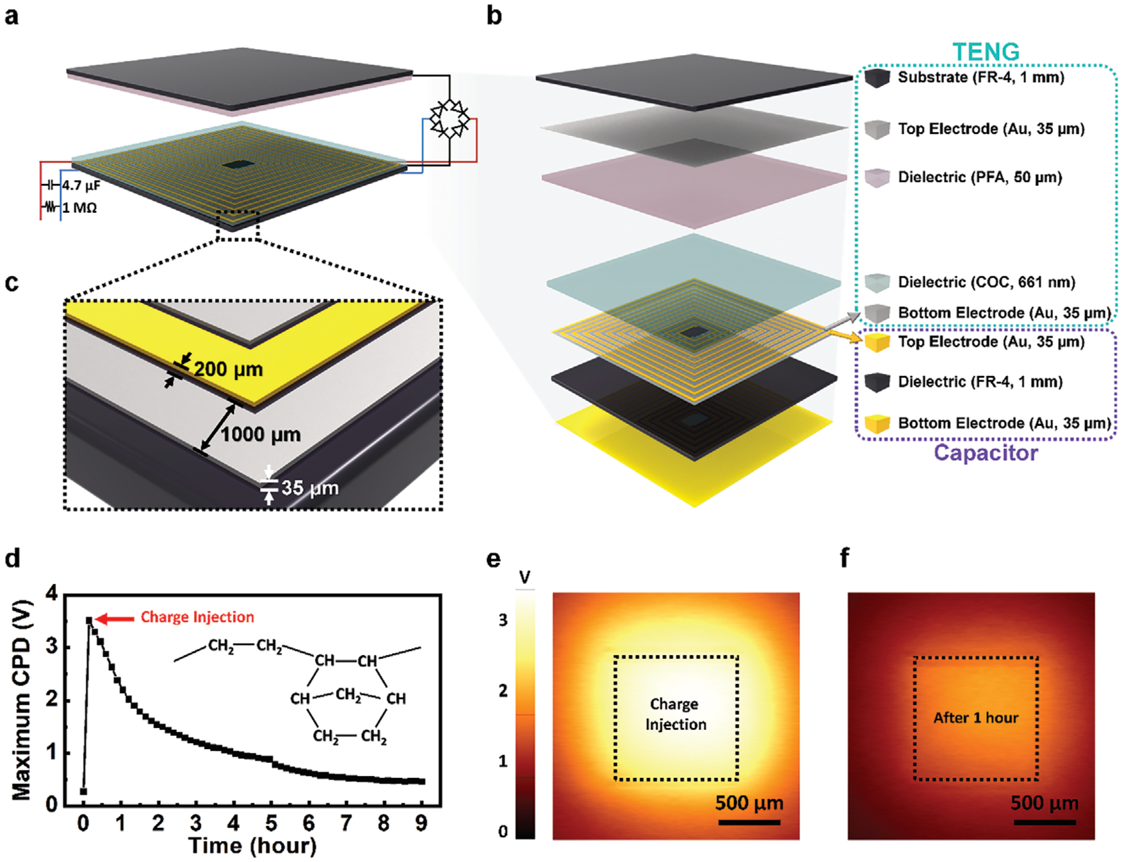

Figure 1. a) TC coupling system and b) each layer. c) Detailed size information of the electrode pattern. d) Maximum CPD values plotted for 9 h after charge injection. KPFM results of COC surface e) immediately after charge injection and f) 1 h after.

environments have been proposed to prevent air breakdown in a high surface charge density state,[27] but these methods also have a limitation in that it is difficult to realize the practical application. As another approach, external charge pumping strategies have been proposed to increase surface charge density by improving charge accumulation processes.[28–34] However, these strategies require an additional external energy source,[28–30] or, for unstable charge pumps, a longer start-up.[31–32]

In this study, we propose an integrated TENG and its capacitive load system that can maximize energy generation and storage efficiency by inducing a coupling effect between the TENG and capacitor by providing specific patterns on the TENG's and capacitor electrodes. The important feature of the TENG–capacitor (TC) coupling system is that the bottom TENG electrode and the top capacitor electrode are located on the same layer. When the TENG output accumulates charges in the top electrode of the capacitor, an additional enhanced electric field is generated around the capacitor electrode. This induces an additional charge transfer between two triboelectric materials. As a result, the enhanced TENG output increases the maximum voltage across the capacitor, thereby the additional electric field from the capacitor. Consequently, the reinforced electric field enhances surface charges on the triboelectric layer again. Therefore, the TC coupling system maximizes the TENG output performance and the voltage of the capacitor. Density functional theory (DFT) calculations were performed to investigate the mechanism of the TC coupling system. Based on the DFT calculation, we observed that the electric field makes the cyclic olefin copolymer (COC) more tribopositive, resulting in additional triboelectric charge transfer between the COC and perfluoroalkoxy alkane (PFA) layers. Additionally, finite element method (FEM) simulations using COMSOL Multiphysics were used to determine the patterning effect and provide optimized pattern designs. Finally, we confirmed experimentally that the energy generation and storage efficiency were enhanced 3 and 3.5 times, respectively, compared with the typical TENG with a separated capacitor system. The results of this work can provide a new platform to achieve high energy generation and storage efficiency for TENGs to be used as portable power sources.

2. Results and Discussion

Figure 1a,b shows the schematic illustration of a TC coupling system and detailed structures of each layer, respectively. The TENG is composed of top and bottom parts having an area of 6 cm × 6 cm; the top part of the TENG has a substrate (FR-4, 1 mm), a top electrode (Au, 35 µm), and a dielectric PFA (50 µm) layer with negative triboelectric characteristics; the bottom part of the TENG has a COC (661 nm) dielectric layer with positive triboelectric characteristics and a patterned bottom electrode (Au, 35 µm).

The embedded fixed capacitor is fabricated in the same layer of the TENG's bottom electrode with a complementary pattern, a thick dielectric (FR-4, 1 mm) and a metal layer (Au, 35 µm) structure, corresponding to the top capacitor electrode, dielectric layer and bottom capacitor electrode, respectively. Here, the most important feature of the TC coupling system is that both the bottom TENG and top capacitor electrodes are located on the same layer and are not in contact. Owing to this unique electrode layout, the top capacitor electrode, which is charged by the TENG output current, can induce a reinforced electric field inside the triboelectric layers when they are in contact, thereby enhancing energy generation efficiency and the charging rate of the capacitor. Based on the charge accumulated model, we developed the displacement current model for the TC coupling system using Maxwell's equation. The displacement current for a conventional TENG can be defined as[35,36,9]

$$J_D = \epsilon \frac{\partial E}{\partial t} + \frac{\partial P_S}{\partial t} \tag{1}$$

where J_D is the displacement current, ϵ is the permittivity of the dielectrics, E is the electric field, and P_S is the polarization field induced by surface polarization charges. $\epsilon \frac{\partial E}{\partial t}$ represents the induced current by the varying electric field, and $\frac{\partial P_S}{\partial t}$ indicates the current caused by the polarization field of surface electrostatic charges. The TC coupling system contains two types of electric fields: the electric field induced by the TENG and that induced by the capacitor. The displacement current for TENG in the TC coupling system can be reorganized as

$$J_D = \epsilon \frac{\partial E_{TENG}}{\partial t} + \epsilon \frac{\partial E_{Cap}}{\partial t} + \frac{\partial P_S}{\partial t} \tag{2}$$

where E_{TENG} is the electric field induced by the TENG, and E_{Cap} is the electric field induced by the capacitor. During the initial stage of the TC coupling system, E_{TENG} contributes to making J_D more dominant than E_{Cap}. After a few cycles of contact separation between triboelectric materials, E_{Cap} is gradually increasing and then begins to contribute to increasing J_D together with E_{TENG}. Finally, enhanced J_D increases E_{Cap} again, creating a virtuous cycle effect.

Detailed size information of the electrode pattern is shown in Figure 1c; the width and thickness of every electrode's finger are 1000 and 35 µm, respectively, and the gap between TENG and capacitor electrodes' finger is 200 µm. Figure 1d shows the chemical structure of COC;[37] and the chemical bonding of COC was evaluated using X-ray photoelectron spectroscopy (XPS),[38] Fourier transform-infrared spectroscopy (FT-IR),[39] and carbon nuclear magnetic resonance spectroscopy (^{13}C NMR)[40] (see Figure S1a–c, Supporting Information). The high surface potential and charge transfer ability of positive triboelectric materials facilitate high output performance of TC coupled TENG. A contact potential difference (CPD) value measured using Kelvin probe force microscope (KPFM) revealed a higher surface potential of COC (408 mV) than that of nylon, a typical positive triboelectric material, (75 mV) (see Figure S2a,b, Supporting Information).[41] Surface charge accumulation and maintaining its potential are other required characteristics for increasing output. We injected the charges into the surface of COC and nylon to investigate the surface charge storage ability of COC and then measured their surface potential for 9 h using atomic force microscopy (AFM). As shown in Figure 1d, although the CPD value decreased from 3.5 to 2.1 V, surface charges were still stored on the COC surface and decreased gradually over 9 h unlike nylon (see Figures S3 and S4, Supporting Information). Figure 1e,f shows the CPD results of the COC surface after immediate charge injection and 1 h after, respectively. The COC can retain surface charges for a long time, which is beneficial for fast charge accumulation on triboelectric layers. Figure S5 (Supporting Information) indicates the TENG output voltage and current density when COC and nylon are used as positive triboelectric material in the TC coupling system, and COC generates high TENG output than nylon.

Figure 2 depicts the working mechanism of the TC coupling system, which increases surface triboelectric charge density at every contact and separation cycle through the coupling effect. The TC coupling system consists of TENG and fixed capacitor parts (Figure 2a and Figure S6, Supporting Information). It also includes a full diode-bridge rectifier to convert the alternating-current (AC) output of TENG into direct-current (DC) output to store energy in the capacitor. The top and bottom electrodes of the TENG are connected to the two AC input lines of the rectifier. The top and bottom electrodes of the capacitor are connected to the positive (V_{out}) and negative (ground) DC outputs of the rectifier, respectively. Assuming both triboelectric layers are initially discharged, when the PFA and COC are first contacted, negative and positive charges are formed on the surface of PFA and COC, respectively, through contact electrification (Figure 2a). When the two triboelectric materials are separated (Figure 2b), electrons move from the top TENG electrode to the bottom capacitor electrode through the diode bridge to compensate for the negative triboelectric charge on the PFA surface (marked by a blue line), and other electrons move from the top capacitor electrode to the bottom TENG electrode through the diode bridge to compensate for the positive triboelectric charge on the COC surface (marked by a red line). As a result, a negative charge forms on the bottom capacitor electrode and a positive charge forms on the top capacitor electrode. When the PFA and COC are in contact again, novel triboelectric charges are generated, and surface charges on the PFA and COC are neutralized. Thereby, the generated charges induced in the top and bottom TENG electrodes flow back (Figure 2c). Electrons move from the top capacitor electrode to the top TENG electrode through the diode bridge (marked by a red line). Other electrons move from the bottom TENG electrode to the bottom capacitor electrode (marked by a blue line). The positive charge stored on the top capacitor electrode forms an electric field, which makes the COC more tribo-positive, resulting in an additional charge transfer between the COC and PFA (Figure 2d). As a result, additional positive and negative charges form on the COC and PFA surface, respectively. When the two triboelectric materials separate and come into contact repeatedly, amplified electrons flow through the same bridge diode paths and amplify movable electrons repeatedly (Figure 2e–h) until the charge saturation of both positive and negative triboelectric layers. In summary, the TENG output charge is stored in an embedded capacitor. Thereby, the positive charge accumulated on the top capacitor electrode induces the electric field that causes additional charge transfer between two triboelectric materials, thus

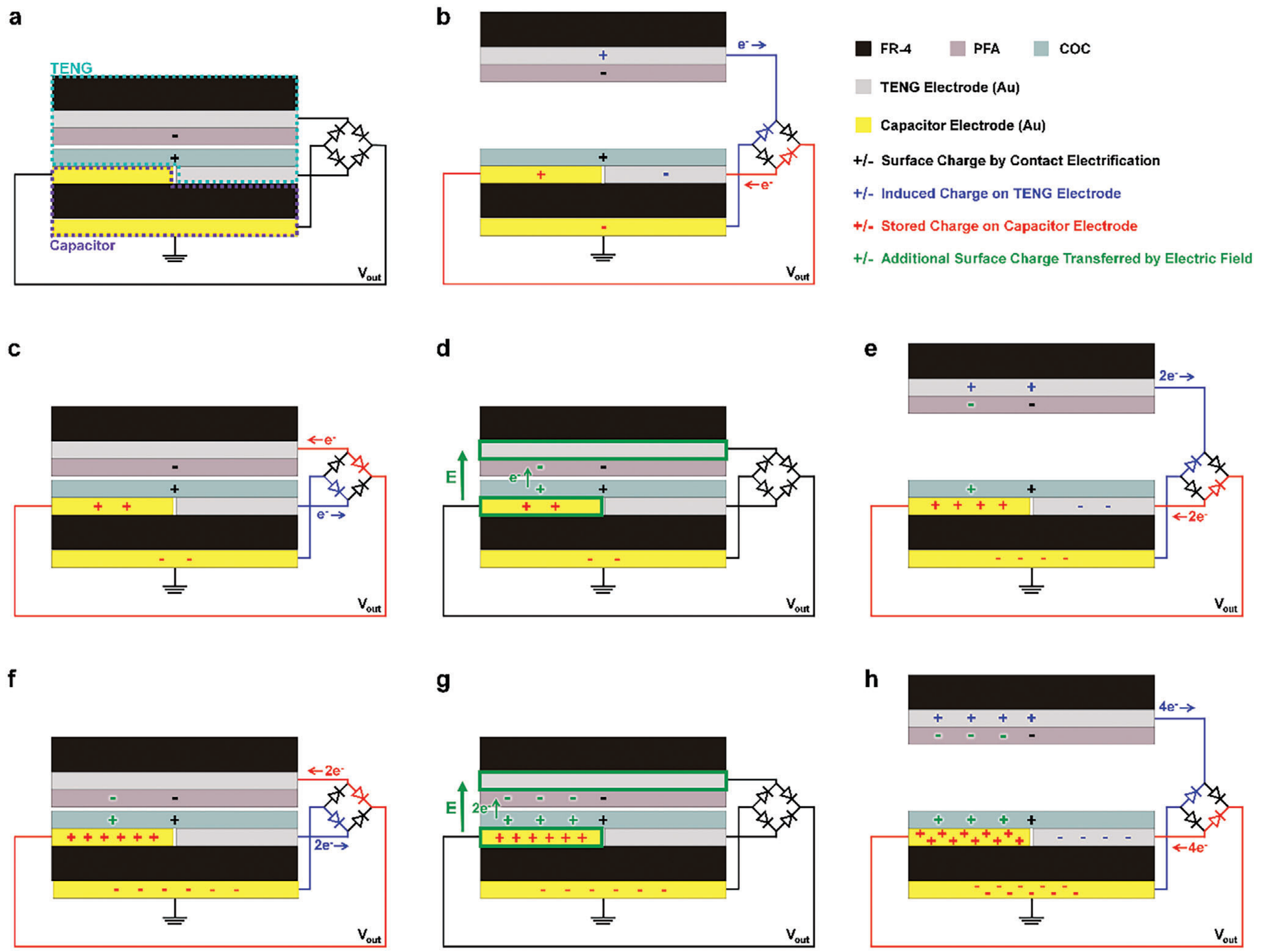

Figure 2. a) Charge transfer on the surface of triboelectric materials based on the contact electrification. b) Opposite charge induction on the top and bottom electrode of TENG based on the electrostatic induction. c) Charge accumulation on the top electrode of capacitor, d) thereby increasing the electric field, which improves the charge transfer between the COC and PFA. e–h) When the two triboelectric materials are separated and in contact repeatedly, amplified electrons flow through the same bridge diode paths and amplify movable electrons repeatedly until the charge saturation of both positive and negative triboelectric layers.

enhancing the triboelectric output and capacitor voltage in virtuous cycles.

To determine the mechanism by which the additional charge transfer between the COC and PFA occurs due to the electric field formed by the positive charge accumulated on the top capacitor electrode to improve the TENG output voltage, we performed a simple basic experiment using a single electrode mode TENG-capacitor system and an external voltage. **Figure 3a** shows the basic experimental setup, where the top triboelectric material of the single electrode mode TENG was PFA (negative). The metal–insulator–metal structure of the capacitor was located below the COC (opposite triboelectric material), and the top and bottom electrode of the capacitor were connected to the positive and negative probes of the power supply to apply the positive voltage to the top capacitor electrode, respectively. When friction occurred, negative and positive charges formed on the surfaces of the PFA and COC by contact electrification, respectively. When applying a positive voltage to the top capacitor electrode, positive charges accumulated on the top capacitor electrode formed the electric field, which made the COC more tribo-positive, resulting in additional charge transfer between the COC and PFA. As a result, additional negative and positive charges formed on the PFA and COC surface, respectively. Therefore, TENG voltage increased as the external voltage applied to the top capacitor electrode increased, as shown in Figure 3b. To investigate the opposite effect, we conducted the same experiment by changing the positions of the PFA and COC (Figure 3c). In this case, when applying the positive voltage to the top capacitor electrode, the electric field formed by the positive charges stored to the top capacitor electrode made the PFA more tribo-positive. Therefore, the TENG voltage decreased as the charge transfer between the COC and PFA decreased. Figure 3d shows the decrease in the TENG voltage as the external voltage applied to the top capacitor electrode increased. Furthermore, we confirmed the TENG output change when applying the positive voltage to the bottom capacitor electrode (Figure S7, Supporting Information). When

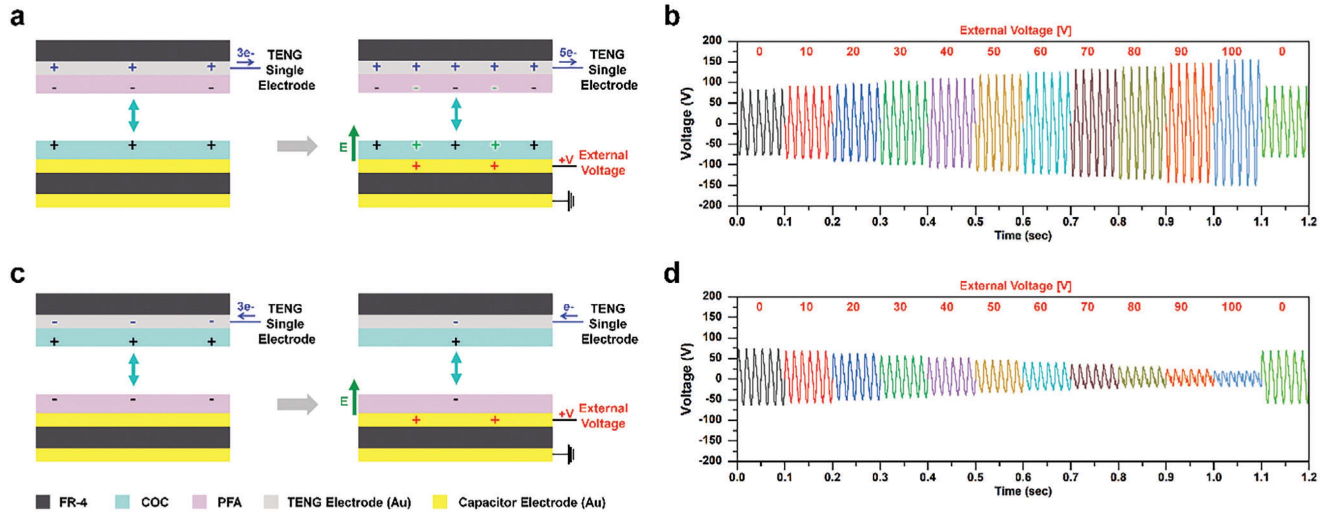

Figure 3. a) Basic experiment setup when the top triboelectric material is PFA (negative) and applying the positive voltage to the top capacitor electrode. b) Increase in TENG voltage with increasing external voltage applied to the top capacitor electrode. c) Basic experiment setup when the top triboelectric material is COC (positive) and applying the positive voltage to the top capacitor electrode. d) Decrease in TENG voltage with increasing external voltage applied to the top capacitor electrode.

applying the positive voltage to the bottom capacitor electrode, the TENG voltage did not change because the positive voltage applied to the bottom capacitor electrode had no effect on the TENG system.

DFT calculations demonstrate the fermi energy changes of COC using external electric fields and charge transfer from PFA to COC. The highest occupied surface state (HOSS) of COC and lowest unoccupied surface state (LUSS) of PFA are critical factors to determine a degree of electron donation and acceptance, respectively.[42] We used the CASTEP module in Materials Studio to optimize the PFA and COC chemical structures to investigate triboelectric behavior of each materials using the density of states and energy band diagram. **Figure** 4a,b shows the LUSS distribution of fluorine atoms in the PFA (highlighted as blue area) and HOSS distribution of hydrogen atoms in the COC (highlighted as red area), respectively. The DFT simulation confirmed a significant change in the fermi energy (i.e., highest electron-occupied energy) through the existence of an external electric field. The change in the fermi energy in the COC increased with the strength of the applied external electric field (Figure S8, Supporting Information). Specifically, the external electric field (0.15 eV $Å^{-1}$ e^{-1}) adjusted the fermi energy of COC from 4.30 to 2.85 eV, which indicated an enhancement of its tribopositive behavior, as shown in Figure 4c. As the fermi energy increases, the work function, which is defined as the distance from the vacuum level to the fermi energy, is anticipated to decrease. These contribute to changes in the energy band structure of COC (Figure S9, Supporting Information). Consequently, this reduction facilitates the movement of electrons from COC to PFA, potentially leading to an increase in charge transfer. Quantitative

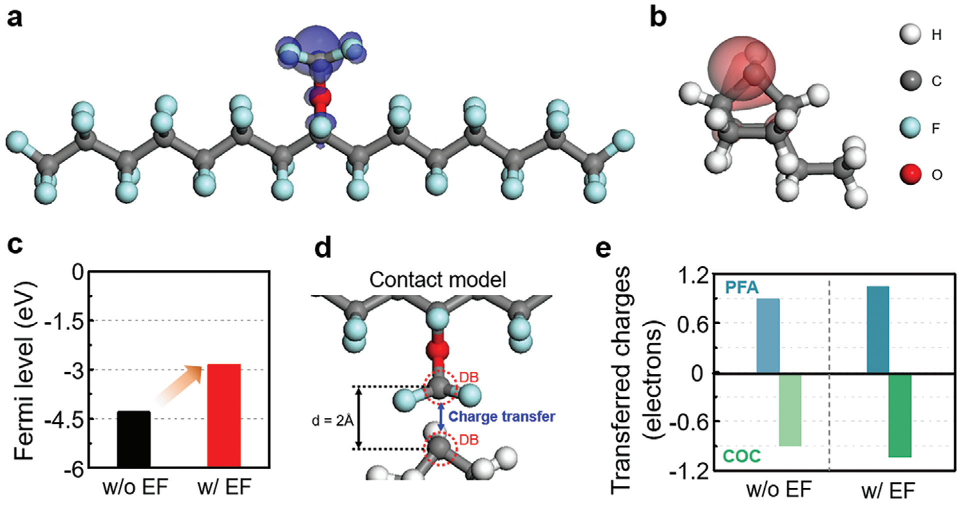

Figure 4. a) LUMO distribution of PFA. b) HOMO distribution of COC. c) Fermi energy of COC without and with an electric field. d) Schematic of the contact model between COC and PFA. e) Amount of transferred electrons of COC and PFA without and with an electric field.

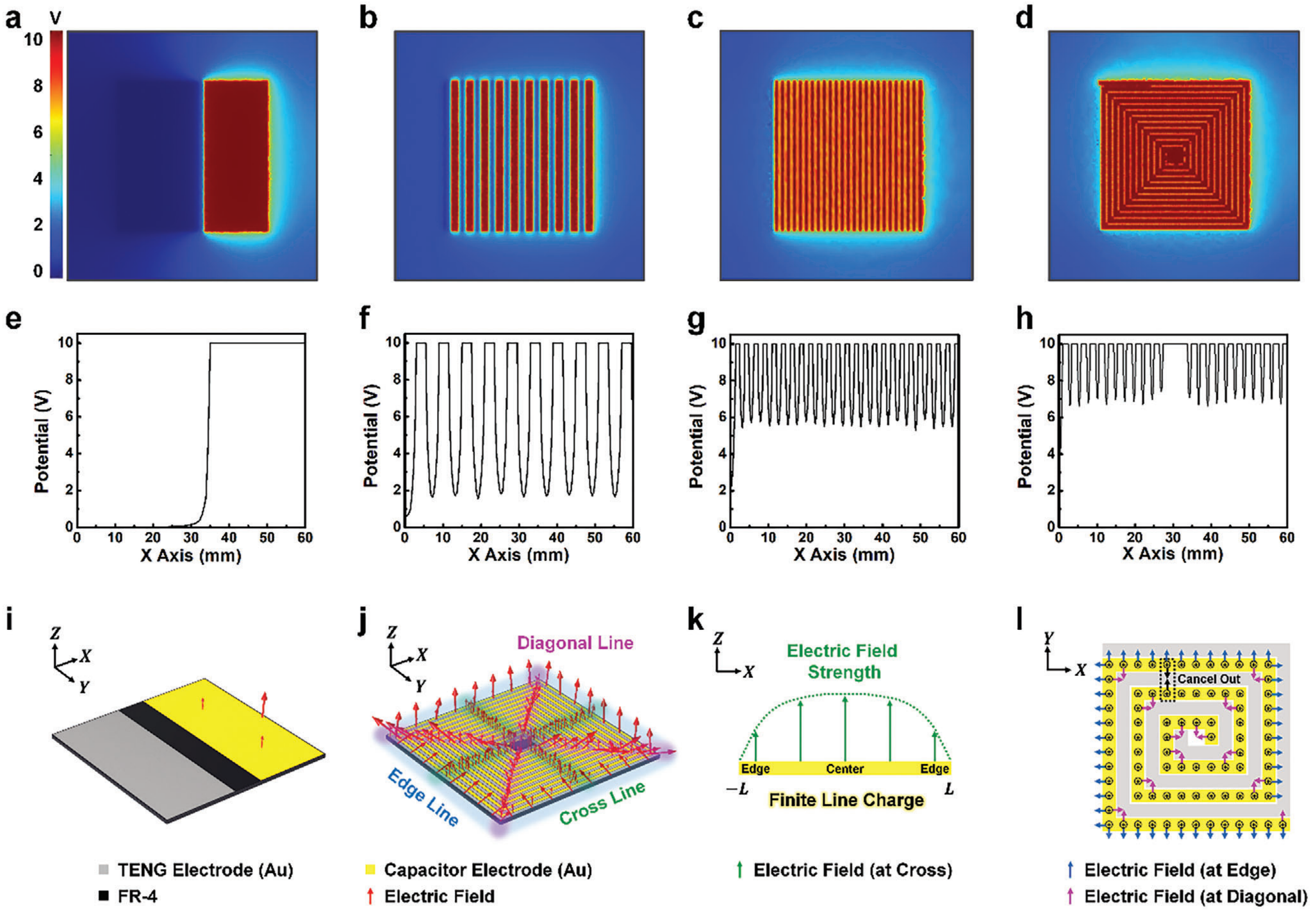

Figure 5. a–d) Potential distribution of four samples with 1-line, 10-line, 25-line, and square electrode patterns on the cross-section view using FEM simulation. e–h) Plotted potential value at the center line of four samples. Illustration of the electric field of i) 1-line and j) square electrode patterns. k) Distribution of electric field along cross line. l) Schematic for calculating the electric field strength generated by two finite line charges at a perpendicular angle.

charge transfer analysis provided additional insight into the effect of the electric field on COC. The charge transfer model between the COC and PFA (Figure 4d) and Mulliken charges was used to analyze the number of transferred electrons (Figure 4e); more charge transfer occurred between COC and PFA from 0.895 to 1.038 when the electric field was applied. This result indicated that the electric field made the COC more tribo-positive, resulting in additional charge transfer between the COC and PFA. Furthermore, we observed that the electric field effect was induced only in the COC with additional charges. Insulators in practical conditions are inevitably subjected to contact with air or other materials, resulting in their electrification. Therefore, it leads to improved output owing to the presence of an electric field.

Potential distribution depends on the electrode patterns. In the TC coupling system, as the positive charges accumulate on the upper electrode of the capacitor, a large electric field is formed. To investigate the electrode pattern effect on the potential distribution, we designed four samples with 1-line, 10-line, 25-line, and square electrode patterns, as shown in Figure S10a–d (Supporting Information), respectively. The bottom electrode of the TENG is shown in grey and the top electrode of the capacitor is shown in yellow. All samples had the same substrate area (3600 mm^2) and total electrode area (3000 mm^2). For the 1-line electrode pattern, the electrode width was 25 mm and the gap between the electrodes was 10 mm. For the 10-line electrode pattern, the electrode width was 2.5 mm and the gap between the electrodes was 0.52 mm. The 25-line and square electrode patterns had the same electrode width of 1 mm and same gap of 0.2 mm. We investigated the potential distribution depending on the electrode pattern via FEM simulation using COMSOL Multiphysics. **Figures** 5a–d and S10e–h (Supporting Information) show the potential distribution of four samples on the top and cross-section view, respectively, when a voltage of 10 V was applied on the top electrode of capacitor. These potentials were distributed over a larger area when the samples had a finer pattern. We plotted the potential value at the center line, as shown in Figure 5e–h. As the line pattern became finer, the mean value of the potential across the center line (without the top electrode of the capacitor) also increased. Interestingly, the square pattern formed a higher potential than the 25-line pattern, although the 25-line and square patterns had the same active area, total electrode area, electrode width, and gap. These results showed that the fine and square patterns had a higher overall potential value owing to the reinforcement interference of the electric field.

To investigate the reinforcement interference of the electric field on the square pattern, we performed additional FEM simulations with COMSOL Multiphysics. We designed the 1-line and square pattern samples and applied the voltage of 10 V to the top capacitor electrode, as shown in Figure 5i,j. The direction and length of the red arrow indicate the direction and intensity of electric field, respectively. The fine square pattern had a stronger electric field distribution than the 1-line pattern owing to the reinforcement interference of the electric field. A strong electric field appeared in the square pattern sample; cross line (highlighted in green), edge line (highlighted in blue), and diagonal line (highlighted in red). Figure 5k shows an example of the distribution of the electric field (highlighted in green) along a finite line charge. When a voltage was applied to the top electrode of the capacitor, a finite line charge was formed in the pattern's lines. The resulting electric fields formed by the finite line charge were superimposed on each other through the superposition principle; thus, the largest electric field was formed at the midpoint. The electric field in Figure 5k is explained by Equation (3), expressing the electric field strength at a point P along the finite line charge (indicated in red in Figure S11a, Supporting Information)[43]

$$\overrightarrow{|E|} = \frac{\lambda}{4\pi\epsilon_0 z}\sqrt{2-2\cos\left\{\tan^{-1}\left(\frac{L+x}{z}\right)+\tan^{-1}\left(\frac{L-x}{z}\right)\right\}} \quad (3)$$

where $\overrightarrow{|E|}$ is the electric field strength, λ is the line charge density, ϵ_0 is the permittivity of free space, L is the half length of the finite line charge, and x and z are the abscissa and ordinate of the point P, respectively. The green curved line in Figure 5k shows that the electric field strength depended on the distance from the center, based on Equation (3); the largest electric field is formed at the midpoint, and the electric field strength decreased as the distance from the center increased. The detailed descriptions are provided in Supporting Information 1.

Figure 5j shows an example of distribution of the electric field at the edge line and diagonal line (highlighted in blue and red, respectively). Owing to the square pattern electrode, the electric field in the xy plane formed at the top electrode of the capacitor was canceled out by another nearby parallel electric field, as shown in Figure 5l (an example is highlighted by the black dotted box). For a finite line charge at the edge line, the electric field was not canceled because there was no other finite line charge existing nearby to the outside, resulting in a strong electric field.

The diagonal line is the point at which two finite line charges with a perpendicular angle connect. At the diagonal line, the electric field did not cancel because no parallel finite line charge exists nearby, but they superimpose on each other from two finite line charges with perpendicular angle. Figure S11b (Supporting Information) shows the superposition of electric fields on the two finite line charges with a perpendicular angle. When two finite line charge occur at a perpendicular angle, Equation (4) shows the electric field vector at the point P, which is affected by finite line charge 1 and 2.[43]

$$\overrightarrow{E_1} + \overrightarrow{E_2} = \frac{\lambda}{4\pi\epsilon_0 x}\left(\sin\alpha_2+\cos\alpha_2\right)\left(\hat{i}+\hat{j}\right) \quad (4)$$

where $\overrightarrow{E_1}$ is the electric field vector formed from a finite line charge 1, $\overrightarrow{E_2}$ is the electric field vector formed from a finite line charge 2, λ is the line charge density, ϵ_0 is the permittivity of free space, α_2 is the angle between the line connecting vertically from the point P to finite line charge and the line connecting to endpoint of the finite line charge, x is the abscissa of the point P, $\hat{i}$ is a unit vector in the x direction, and $\hat{j}$ is a unit vector in the y direction. The largest electric field is formed at the diagonal line at which two finite line charges connect to each other at a perpendicular angle. The detailed description is provided in Supporting Information 2.

To confirm the enhancement of output performance of a TENG by the TC coupling effect, we measured the triboelectric output voltage, current, and capacitor charge behaviors of the three types of systems: a typical TENG (case 1), a TENG-capacitor separation system (case 2), and the equivalent TC coupling system (case 3). **Figures** 6a and S12a (Supporting Information) show a typical setup where the TENG was directly connected to a diode bridge loaded with the TC capacitor in parallel with a 4.7 µF capacitor and a 1 MΩ resistor. For an equivalent comparison with the TC coupling system, both top and bottom TENG electrodes were fully filled flat electrodes; all materials and dimension were as same as for the TC coupling system; the 1 MΩ resistor acted as an overall circuit impedance of future application. Figure 6b and Figure S12b (Supporting Information) depict the TENG-capacitor separation system with the same structure as case 1, but only the co-exist of the bottom TENG and top capacitor electrode differed; the top capacitor electrode was disconnected from the system. The TC coupling system is also connected to a 4.7 µF capacitor and a 1 MΩ resistor load (see Figure 6c and Figure S12c, Supporting Information). Figure 6d–f shows the triboelectric output voltage, current, and load voltage of the three types of systems, respectively. As described above, the enhanced electric field by TC coupling effect increased the output voltage over ≈3 times higher than others. A comparison with the typical TENG and variously patterned TC coupling systems is shown in Figure 6g–i and Figures S13–S19 (Supporting Information). It provides clear evidence of the TC coupled electric field enhancements effects. Even if the 25-line and square patterned electrode designs had the same length of electrode and parasitic capacitance, the enhancement of electric field at corners in the square patterned electrode design was a dominant factor in increasing the output performance. Figure S20 (Supporting Information) indicates RMS current density and RMS power density depending on the external load. The TC coupling system exhibited its maximum power density of 47 W m^{-2} at the external load of 1 MΩ. Long-term stability of the TENG output voltage was verified during 15 000 operation cycles (Figure S21, Supporting Information).

3. Conclusion

In this study, we developed a TC coupled system that can achieve higher output performance and enhanced energy storage capability than a typical TENG system by integrating the TENG and capacitor. The design of a fine square pattern at the bottom TENG electrode and top capacitor electrode generates an amplified electric field near the top capacitor electrode, thereby inducing high surface charge density in the triboelectric layer. DFT calculations confirmed that the fermi energy of the COC increases when the

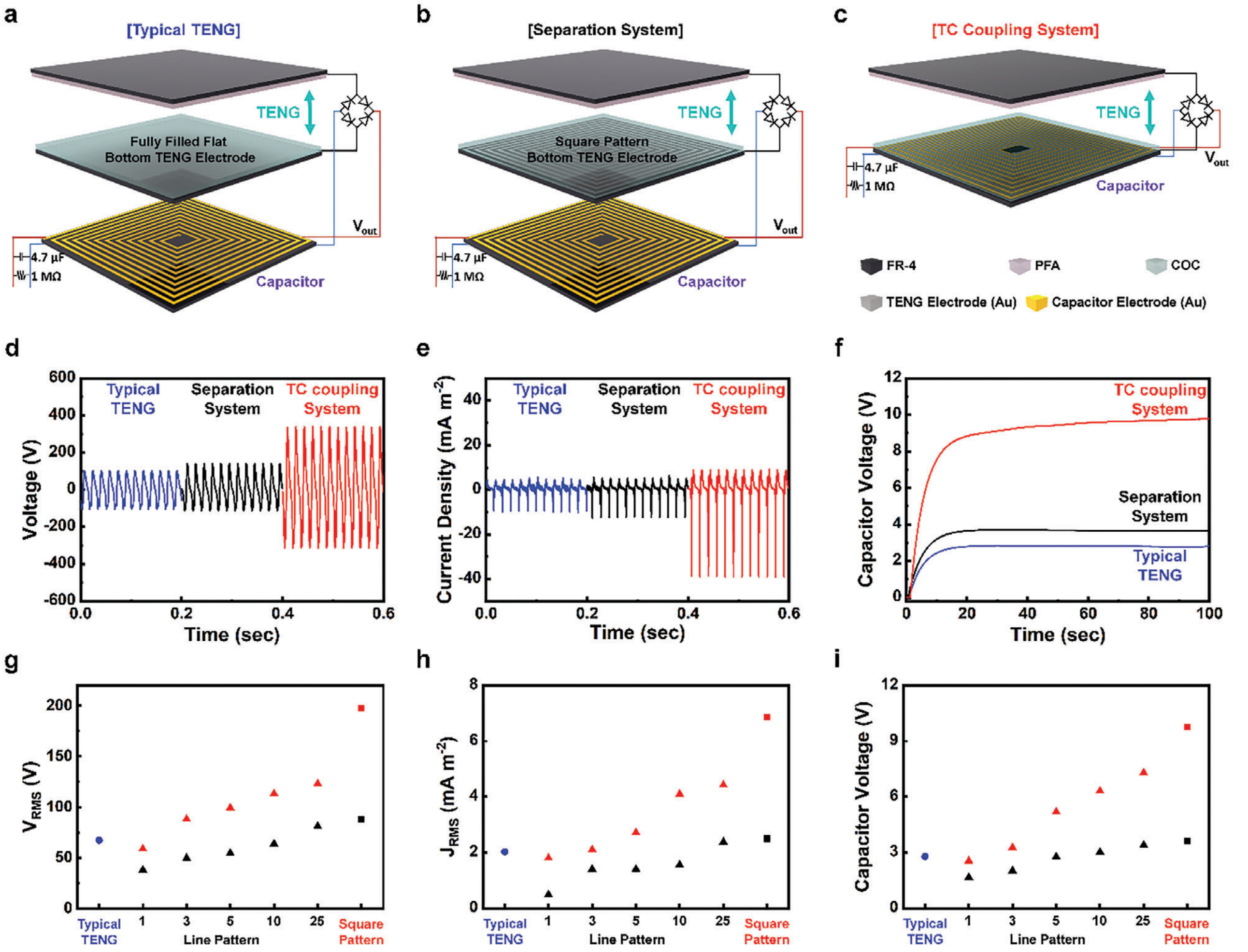

Figure 6. Schematic of a) typical TENG with the separated capacitor, b) separation system in which the TENG and capacitor are separated, and c) TC coupling system. d) Triboelectric voltage, e) current, and f) capacitor voltage of typical TENG (marked in blue), separation system (marked in black), and TC coupling system (marked in red). g) RMS triboelectric voltage, h) RMS triboelectric current density, and i) capacitor voltage of three types systems; typical TENG (marked in blue), separation system (marked in black), and TC coupling system (marked in red) depending on the line and square electrode patterns.

electric field induced on the top capacitor electrode is applied, resulting in more charge transfer between the two triboelectric materials. Therefore, the enhanced TENG output power, resulting from a TC coupling effect, increases the maximum capacitor voltage that induces an additionally strengthen electric field in virtuous cycles. FEM simulation of electric field and output performances of TENGs for various electrode patterns provided a clear understanding of the TC coupling effect. This study can provide a new platform for a high-performance TENG without being limited by materials and additional external power sources, and specifically, the TC coupling effect can be utilized as a miniaturized power source and suggest significant directions for TENG structural design.

4. Experimental Section

Fabrication and Characterization: The TENG and capacitor structure were fabricated using a PCB fabrication process. The PFA film was attached to a Au electrode using a carbon double side tape. The COC solution was prepared by dissolving COC particles (6013S-04, TOPAS Advance Polymers) in toluene solvent (244 511, Sigma-Aldrich) by stirring (10 wt%) for 24 h at room temperature (25 °C). Thereafter, the COC solution was coated on a substrate using spin coater (2000 rpm, 60 s), followed by drying at 80 °C for 9 h in an oven and cooling naturally to prevent thermal damage. XPS (ESCALAB250, Thermo-Scientific), FT-IR (TENSOR27, Bruker IFS-66/S), and ^{13}C NMR (Varian Technology, Unity Inova) measurements were performed to confirm the chemical bonding of the COC. For KPFM (XE-100, Park Systems) measurements, the COC and nylon were prepared on a stainless steel holder and measured under a set point of 13 nm at a scan rate of 0.5 Hz (temperature = 21 °C, humidity = 17%). KPFM measurements were performed using a Pt/Cr-coated silicone tip, lock-in amplifier (SR830, Stanford Research), and 2 V_{ac} signal at a frequency of 17 kHz. For the surface charge storage ability of COC and nylon, a 20 V bias was applied to the Pt tip of AFM and scratched the center of the COC and nylon surface using a Pt tip. Subsequently, the CPD value was measured every hour for 9 h to confirm the change in surface potential. For the TENG characterizations, a shaker (Model No. ET-126B-4, Labworks Inc.), digital phosphor oscilloscope (DPO 3052 Digital Phosphor, Tektronix), and low-noise current pre-amplifier (Model No. SR570, Stanford Research Systems, Inc.) were used. The electric field distribution was simulated by the finite element method using COMSOL Multiphysics.

DFT Calculation: DFT calculations were performed using the CASTEP software from Materials Studio. The geometry of PFA and COC structures were optimized using the Perdew, Burke, and Ernzerhof exchange–correlation potential with the generalized gradient approximation and the BFGS minimization algorithm. While the geometry optimization was progressed, energy, force, and displacement tolerances were set at 1×10^{-5} eV atom^{-1}, 0.03 eV Å^{-1}, and 0.001 Å, respectively. Additionally, the on-the-fly generation ultrasoft was used as pseudopotential and All Bands method was used as an electronic minimizer to improve the accuracy of minimized-energy structure calculations. To model the dangling bonds in PFA and COC structure, the spin of unpaired electrons was optimized using collinear spin polarization. To investigate the charge transfer of electron between PFA and COC in response to an electric field, the electron density difference of a set of atoms was measured. During this calculation, to clarify the charge transfer, the authors applied an additional electron charge in the COC and a high value of external electric field (0.15 eV Å^{-1} e^{-1}) to investigate the electric field effect more clearly.

Supporting Information

Supporting Information is available from the Wiley Online Library or from the author.

Acknowledgements

J.K., H.R., and S.M.K. contributed equally to this work. This work was supported by the Basic Science Research Program (2022R1A3B107829), the Bio & Medical Technology Development Program (2022M3E5E9082206), and the Original Technology Development Program (2021M3E8A2100391) through the National Research Foundation of Korea (NRF) funded by the Korean government (MSIT). S.-W.K. acknowledges the Yonsei World-Class Fellow Program funded by Y. J. Lee.

Conflict of Interest

The authors declare no conflict of interest.

Data Availability Statement

The data that support the findings of this study are available from the corresponding author upon reasonable request.

Keywords

capacitor, coupling, density functional theory, energy harvesting, triboelectric nanogenerator

Received: August 7, 2023
Revised: January 7, 2024
Published online:

---

[1] S. Chu, A. Majumdar, *Nature* **2012**, *488*, 294.
[2] E. J. Markvicka, M. D. Bartlett, X. Huang, C. Majidi, *Nat. Mater.* **2018**, *17*, 618.
[3] Z. Zhou, K. Chen, X. Li, S. Zhang, Y. Wu, Y. Zhou, K. Meng, C. Sun, Q. He, W. Fan, E. Fan, Z. Lin, X. Tan, W. Deng, J. Yang, J. Chen, *Nat. Electron.* **2020**, *3*, 571.
[4] R. Hinchet, H.-J. Yoon, H. Ryu, M.-K. Kim, E.-K. Choi, D.-S. Kin, S.-W. Kim, *Science* **2019**, *365*, 491.
[5] W. Xu, H. Zheng, Y. Liu, X. Zhou, C. Zhang, Y. Song, X. Deng, M. Leung, Z. Yang, R. X. Xu, Z. L. Wang, X. C. Zeng, Z. Wang, *Nature* **2020**, *578*, 392.
[6] Z. L. Wang, *Mater. Today* **2017**, *20*, 74.
[7] F.-R. Fan, Z.-Q. Tian, Z. L. Wang, *Nano Energy* **2012**, *1*, 328.
[8] S. Niu, S. Wang, Y. Liu, Y. S. Zhou, L. Lin, Y. Hu, K. C. Pradel, Z. L. Wang, *Energy Environ. Sci.* **2014**, *7*, 2339.
[9] Z. L. Wang, *Nano Energy* **2020**, *68*, 104272.
[10] Z. L. Wang, *Adv. Energy Mater.* **2020**, *10*, 2000137.
[11] Z.-Y. Huo, Y.-J. Kim, I.-Y. Suh, D.-M. Lee, J. H. Lee, Y. Du, S. Wang, H.-J. Yoon, S.-W. Kim, *Nat. Commun.* **2021**, *12*, 3693.
[12] H. Ryu, H.-M. Park, M.-K. Kim, B. Kim, H. S. Myoung, T. Y. Kim, H.-J. Yoon, S. S. Kwak, J. Kim, T. H. Hwang, E.-K. Choi, S.-W. Kim, *Nat. Commun.* **2021**, *12*, 4374.
[13] H.-J. Yoon, M. Kang, W. Seung, S. S. Kwak, J. Kim, H. T. Kim, S.-W. Kim, *Adv. Energy Mater.* **2020**, *10*, 2000730.
[14] J. Kim, H. Cho, M. Han, Y. Jung, S. S. Kwak, H.-J. Yoon, B. Park, H. Kim, H. Kim, J. Park, S.-W. Kim, *Adv. Energy Mater.* **2020**, *10*, 2002312.
[15] J. Kim, J. H. Lee, H. Ryu, J.-H. Lee, U. Khan, H. Kim, S. S. Kwak, S.-W. Kim, *Adv. Funct. Mater.* **2017**, *27*, 1700702.
[16] J. Wang, S. Li, F. Yi, Y. Zi, J. Lin, X. Wang, Y. Xu, Z. L. Wang, *Nat. Commun.* **2016**, *7*, 12744.
[17] H. Zheng, A. Zhou, Y. Li, X. Chen, Y. Chen, Y. Xu, Y. Li, H. Ge, X. Ning, *Nano Energy* **2023**, *113*, 108529.
[18] D.-L. Wen, P. Huang, H.-T. Deng, X.-R. Zhang, Y.-L. Wang, X.-S. Zhang, *Microsyst. Nanoeng.* **2023**, *9*, 94.
[19] H.-T. Deng, D.-L. Wen, J.-R. Liu, X.-R. Zhang, Y.-L. Wang, P. Huang, B. Kim, X.-S. Zhang, *Nano Res.* **2023**, *16*, 7618.
[20] Y.-Y. Ba, J.-F. Bao, X.-T. Liu, X.-W. Li, H.-T. Deng, D.-L. Wen, X.-S. Zhang, *J Reticuloendothel Soc* **2021**, *2021*, 9817062.
[21] W. Seung, H.-J. Yoon, T. Y. Kim, H. Ryu, J. Kim, J.-H. Lee, J. H. Lee, S. Kim, Y. K. Park, Y. J. Park, S.-W. Kim, *Adv. Energy Mater.* **2017**, *7*, 1600988.
[22] S. S. Kwak, S. M. Kim, H. Ryu, J. Kim, U. Khan, H.-J. Yoon, Y. H. Jeong, S.-W. Kim, *Energy Environ. Sci.* **2019**, *12*, 3156.
[23] J. Kim, H. Ryu, J. H. Lee, U. Khan, S. S. Kwak, H.-J. Yoon, S.-W. Kim, *Adv. Energy Mater.* **2020**, *10*, 1903524.
[24] C. Yao, X. Yin, Y. Yu, Z. Cai, X. Wang, *Adv. Funct. Mater.* **2017**, *27*, 1700794.
[25] S. Wang, Y. Zi, Y. S. Zhou, S. Li, F. Fan, L. Lin, Z. L. Wang, *J. Mater. Chem. A* **2016**, *4*, 3728.
[26] S. Wang, Y. Xie, S. Niu, L. Lin, C. Liu, Y. S. Zhou, Z. L. Wang, *Adv. Mater.* **2014**, *26*, 6720.
[27] J. Wang, C. Wu, Y. Dai, Z. Zhao, A. Wang, T. Zhang, Z. L. Wang, *Nat. Commun.* **2017**, *8*, 88.
[28] Y. Li, Z. Zhao, L. Liu, L. Zhou, D. Liu, S. Li, S. Chen, Y. Dai, J. Wang, Z. L. Wang, *Adv. Energy Mater.* **2021**, *11*, 2100050.
[29] W. Liu, Z. Wang, G. Wang, G. Liu, J. Chen, X. Pu, Y. Xi, X. Wang, H. Guo, C. Hu, Z. L. Wang, *Nat. Commun.* **2019**, *10*, 1426.
[30] H. Wang, L. Xu, Y. Bai, Z. L. Wang, *Nat. Commun.* **2020**, *11*, 4203.
[31] A. Ghaffarinejad, J. Y. Hasani, R. Hinchet, Y. Lu, H. Zhang, A. Karami, D. Galayko, S.-W. Kim, P. Basset, *Nano Energy* **2018**, *51*, 173.
[32] M. A. B. Ouanes, H. Samaali, D. Galayko, P. Basset, F. Najar, *Nano Energy* **2019**, *62*, 465.
[33] A. N. Ravichandran, M. Ramuz, S. Blayac, *Adv. Mater. Technol.* **2020**, *5*, 2000650.
[34] L. Xu, T. Z. Bu, X. D. Yang, C. Zhang, Z. L. Wang, *Nano Energy* **2018**, *49*, 625.
[35] Z. L. Wang, T. Jiang, L. Xu, *Nano Energy* **2017**, *39*, 9.
[36] Z. L. Wang, *Mater. Today* **2017**, *20*, 74.
[37] S.-J. Hwang, M.-C. Tseng, J.-R. Shu, H. H. Yu, *Surf. Coat. Technol.* **2008**, *202*, 3669.

[38] S. Roy, C. Y. Yue, Y. C. Lam, Z. Y. Wang, H. Hu, *Sens. Actuators, B* **2010**, *150*, 537.

[39] G. Schelcher, C. Guyon, S. Ognier, S. Cavadias, E. Martinez, V. Taniga, L. Malaquin, P. Tabeling, M. Tatoulian, *Lab Chip* **2014**, *14*, 3037.

[40] L. Boggioni, N. G. Galotto, F. Bertini, I. Tritto, *Polymers* **2016**, *8*, 60.

[41] K. Y. Lee, S. K. Kim, J.-H. Lee, D. Seol, M. K. Gupta, Y. Kim, S.-W. Kim, *Adv. Funct. Mater.* **2016**, *26*, 3067.

[42] J. Kim, D. Kang, H.-K. Lee, J.-H. Hwang, H. Y. Lee, S. Jeon, D. Kim, S. M. Kim, S.-W. Kim, *Adv. Funct. Mater.* **2023**, *33*, 2209648.

[43] R. K. Wangsness, *Electromagnetic Fields*, 2nd ed., Wiley, Hoboken, NJ **1991**.